



UNIVERSITY OF LEEDS

This is a repository copy of *Simulation of Intermetallic Solidification using Phase-Field Techniques*.

White Rose Research Online URL for this paper:
<http://eprints.whiterose.ac.uk/135708/>

Version: Accepted Version

Article:

Mullis, AM orcid.org/0000-0002-5215-9959, Bollada, PC and Jimack, PK (2018) Simulation of Intermetallic Solidification using Phase-Field Techniques. Transactions of the Indian Institute of Metals, 71 (11). pp. 2617-2622. ISSN 0972-2815

<https://doi.org/10.1007/s12666-018-1428-3>

© The Indian Institute of Metals - IIM 2018. This is a post-peer-review, pre-copyedit version of an article published in Transactions of the Indian Institute of Metals. The final authenticated version is available online at: <https://doi.org/10.1007/s12666-018-1428-3>.

Reuse

Items deposited in White Rose Research Online are protected by copyright, with all rights reserved unless indicated otherwise. They may be downloaded and/or printed for private study, or other acts as permitted by national copyright laws. The publisher or other rights holders may allow further reproduction and re-use of the full text version. This is indicated by the licence information on the White Rose Research Online record for the item.

Takedown

If you consider content in White Rose Research Online to be in breach of UK law, please notify us by emailing eprints@whiterose.ac.uk including the URL of the record and the reason for the withdrawal request.



eprints@whiterose.ac.uk
<https://eprints.whiterose.ac.uk/>

Simulation of Intermetallic Solidification using Phase-Field Techniques

A.M. Mullis¹, P.C. Bollada¹ & P.K. Jimack²

¹School of Chemical & Process Engineering, University of Leeds, Leeds LS2 9JT UK.

²School of Computing, University of Leeds, Leeds LS2 9JT UK.

Keywords: Intermetallic compounds, solute trapping, faceted crystals, thermodynamics.

Abstract

We present current ideas towards developing a phase-field model appropriate to the solidification of intermetallic phases. Such simulation presents two main challenges (i) dealing with faceted interfaces and (ii) the complex sub-lattice models used to describe the thermodynamics of such phases. Although models are already existent for the simulation of faceted crystals, some of these can be shown to produce highly unrealistic Wulff shapes. The model present here uses a parameterization of the Wulff shape as a direct input to the model, allowing the simulation of arbitrary crystal shapes. In addition, an anti-trapping current that can be used with arbitrary (including sub-lattice) thermodynamics is presented. Such anti-trapping currents are vital in the simulation of intermetallic phases where the steep liquidus slope means small deviations in solute partitioning behaviour can translate to a significant change in tip undercooling.

1.0 Introduction

Phase-field modelling is one of the best established and most widely used tools for microstructural simulation of materials, with numerous authors now using the technique to simulate a wide range of morphologies including dendritic, eutectic, peritectic and monotectic structures. Despite this, as soon as we move away from solution type phases with a continuous interface, such modelling becomes decidedly non-trivial. Specifically, the modelling of intermetallic phases is problematic. Such phases have widespread metallurgical interest; as promising structural materials in their own right and as both desirable and undesirable inclusions in solid-solution alloys. Some of the challenges associated with the modelling of intermetallics include: complex thermodynamic phase descriptions, particularly for non-stoichiometric phases, faceted interfaces and very steep liquidus lines.

For non-stoichiometric intermetallics the standard CALPHAD description of their free energy is via a sublattice model. The sublattice model can be explained with reference to an intermetallic such as AlNi. The model for AlNi contains two sub-lattices, which we write as (Al,Ni)(Ni,Va), i.e. the first sub-lattice contains one site which can be occupied by either an Al atom or an Ni atom, the second sub-lattice contains one site which can be occupied by an Ni atom or which can remain as a vacancy. This gives site occupancy fractions y'_{Al} , y'_{Ni} , y''_{Ni} and y''_{Va} which map uniquely onto the concentration c . Here, y' denotes n site occupancy on the first sublattice and y'' a site occupancy on the second sublattice. For $c < 0.5$ the first sub-

lattice is fully occupied by Al atoms, with vacancies on the second sub-lattice to give the correct c . For $c > 0.5$ the second sub-lattice is fully occupied by Ni atoms, with some additional Ni atoms also on the first sub-lattice. The free energy for a sublattice phase is typically given by a weighted sum over the product of all unique pairs of site occupancy fractions (see Section §2.1 below), together with entropy of mixing terms. The necessary weights for the site occupancy product pairs will typically be accessed via a thermodynamic database, such as that maintained by SGTE [1], which is itself based on published thermodynamic assessments. Such data is available for most binary intermetallics (at least for the more common elements). However, coverage is much more patchy for ternary and higher order intermetallics. To date, most phase-field models that attempt to use such complex thermodynamic models [e.g. 2, 3] do so by coupling directly to a CALPHAD engine such as ThermoCalc to look up the free energy of the desired phases in the vicinity required and then making a quadratic approximation to these (in the composition variable, c) to actually work with. However, this requires multiple calls to the CALPHAD engine on each iteration, resulting in a potentially large computational overhead.

Considering the profusion of papers published on phase-field techniques over the past 20 years, relatively few of them deal with the growth of faceted crystals. In large part this reflects the natural contradiction of introducing discontinuities in the crystal morphology when the whole rationale of the phase-field technique is to blur the solid-liquid interface in order that the system is everywhere differentiable. Despite this, various phase-field methodologies have been proposed for capturing faceted growth [e.g. 4, 5, 6]. Most of these rely on some form of regularization of the crystal shape, typically replacing sharp corners (discontinuous changes in growth direction) with slightly rounded-off versions of the same. However, even where such models have been developed this has mainly been stimulated by interest in the crystallization of the semiconductors Si and Ge. Very little attention has been focused on the concurrent growth of a faceted and a continuous phase, as may for instance occur during the growth of intermetallics at the grain boundaries of a solid-solution alloy. An example of such would be the growth of θ -Al₁₃Fe₄ in Al-alloys contaminated with Fe, this being a serious issue for Al producers due to the deleterious mechanical properties imparted by the θ -phase.

An alternative approach which has shown considerable promise in the simulation of faceted morphologies is the so called Extended Cahn-Hilliard Model (ECHM), in which, rather than introducing the crystallographic anisotropy via an orientation depended coefficient, ϵ , to the gradient energy, higher order tensorial gradient energy terms are introduced [7]. The approach has a number of advantages, including that the stationary crystal shape does not exhibit sharp corners [8, 9] even when the interfacial energy is high enough for the corresponding Wulff shape to do so. However, here we have adopted a pragmatic view and used a regularised conventional phase-field model, due to the extensive literature on extending such models to multi-phase systems.

A further challenge in attempting to make quantitative simulation of intermetallic growth is the steep liquidus lines often associated with such phases. Returning to the example of θ -Al₁₃Fe₄, at the α - θ eutectic on the Al-rich side of the phase diagram the gradient of the θ -

liquidus line is 131 K/at.%. This is important because, unless correct, all phase-field models suffer from artificial solute-trapping, which means that the local partition coefficient, $k = c_s^*/c_l^*$, departs from its equilibrium value, $k_E = c_s^E/c_l^E$ (here, c_s^* and c_l^* are the actual solute concentrations at the solid-liquid interface in the solid and liquid respectively while c_s^E and c_l^E are the equivalent values from the equilibrium phase diagram), becoming closer to unity than the equilibrium value. While this can be an issue for all phase types, the problem is particularly pertinent for intermetallics as the steep slope of the liquidus line means that small errors in the solute concentration at the tip map on to large errors in the tip undercooling. Typically, such artificial solute trapping is correct by the use of anti-trapping currents, the best known of which is that due to Karma [10]. However, most such currents are derived on the basis of highly simplified thermodynamics (ideal solutions, linear liquidus and solidus lines, constant k_E) and as such are unsuitable for use with complex sublattice models used to describe the thermodynamics of intermetallic phases. We are aware of only one previous attempt [2] to develop an anti-trapping for use with arbitrary thermodynamics, although even here it was actually applied to quadratic approximations of the free energy obtained from a CALPHAD engine.

Recently, Galenko and co-workers [11] have suggested that solute trapping in phase-field models of solidification should be modelled by a hyperbolic, rather than parabolic, transport equation in order to account for the finite velocity of the solute atoms. Such hyperbolic equations can also be formulated for thermal transport [12]. The hyperbolic model can in turn be used to calibrate the appropriate level of solute trapping within a parabolic phase-field model with finite interface dissipation [13]. However, given the lack of such hyperbolic simulations for complex intermetallic phases we adopt, as above, the pragmatic approach of using a conventional parabolic transport model.

2.0 Development of a Phase-Field Model for Intermetallic Solidification

We start with a standard phase-field model in which the evolution of the phase variable, ϕ , which takes values 0 in the solid and 1 in the liquid, is given by:

$$\dot{\phi} = -M \frac{\delta F}{\delta \phi} \quad (1)$$

where M is the mobility. F is given by:

$$F = \int_{\Omega} f(\phi, \nabla \phi, c) dx^3 \quad (2)$$

where f is the free energy density:

$$f = H(c) \left[\gamma^2 (\nabla \phi)^2 \delta^2 \nabla \phi \cdot \nabla \phi + \phi^2 (1 - \phi)^2 \right] + G(\phi, c, T) \quad (3)$$

Here, $H(c)$ is a barrier height for the standard double-well potential used in phase-field modelling to localise ϕ to values of 0 or 1, with δ the interface width and γ a function that describes the surface energy anisotropy. G is the bulk free energy, which is interpolated between the values for the pure phases. **The self-consistency of the model employed has previously been demonstrated in [14].**

The evolution of the solute field, c , including an arbitrary (and as yet unspecified) anti-trapping current, \mathbf{j} , is conventionally given by:

$$\dot{c} = -\nabla \cdot \left(D \nabla \frac{\delta F}{\delta c} + \mathbf{j} \right) = -\nabla \cdot (D \nabla f_c + \mathbf{j}) \quad (4)$$

With D being the solute diffusivity, which is typically interpolated between the values for the pure solid, D_s , and the pure liquid, D_l , via $D = \phi D_l + (1 - \phi) D_s$.

Numerical solutions to the equation set are obtained using the computational framework described in [15]. We use a cell centred finite difference mesh, with standard stencils for the first and second derivatives and a compact stencil for the Laplacian (9 point in 2-D, 27 point in 3-D). The mesh employs dynamic adaptivity to concentrate mesh cells in the vicinity of the solid liquid interface, with the refinement/derefinement criteria based upon a weighted sum of the gradients of ϕ and c . Temporal discretisation is via an implicit, second order backward difference scheme with variable time step. The resulting set of large but sparse non-linear algebraic equations is solved via a multigrid scheme employing a pointwise Jacobi smoother within the Full Approximation Scheme (FAS) [16]. Dynamic load balancing for parallel execution is performed using the PARAMESH [17] package, although the coarse grid bottleneck in the multigrid scheme means that 64-256 are typically optimal.

2.1 Sublattice Thermodynamics

The bulk thermodynamics of the system appear in the model via the term $G(\phi, c, T)$ in Equation (3). Typically, for the liquid and solid-solution phases the free energy will be a linear interpolation of the end members together with contributions for the entropy and excess free energy of mixing. Returning to the Al-Ni case we would have:

$$G_j(c, T) = c G_j^{Ni}(T) + (1 - c) G_j^{Al}(T) + \frac{RT}{v_m} [c \ln c + (1 - c) \ln(1 - c)] + G_j^{xs}(c, T) \quad (5)$$

where j label the pure phase, R is the gas constant and v_m the molar volume. The G_j^{Ni} and G_j^{Al} are given by piecewise continuous expansions of the form:

$$G_j^X = a_j^X + b_j^X T + c_j^X T \ln T + d_j^X T^2 + e_j^X T^3 + f_j^X T^{-1} + g_j^X T^7 + h_j^X T^{-9}, \quad X = \text{Al or Ni} \quad (6)$$

with the coefficients $a-h$ being obtained from a thermodynamic database, we use SGTE 5.0. For the G_j^{xs} is the excess free energy of mixing given by a Redlich-Kister [18] model, which including terms up to 4th order would be:

$$G_j^{xs}(c) = c(1-c) \sum_{m=0}^4 (p_j^{(m)} + q_j^{(m)}T) (1-2c)^m \quad (7)$$

Again, the coefficients p and q may be obtained from a thermodynamic database such as SGTE.

For the sublattice intermetallic phases rather more complex expressions involving the site occupancy fractions arise. Taking the B2 AlNi phase as an example, we have:

$$\begin{aligned} (1 + y''_{Ni})G_{AlNi} = & y'_{Al}y''_{Ni}G_{Al:Ni}^{AlNi} + y'_{Al}y''_{Va}G_{Al:Va}^{AlNi} + y'_{Ni}y''_{Ni}G_{Ni:Ni}^{AlNi} + y'_{Ni}y''_{Va}G_{Ni:Va}^{AlNi} \\ & + RT \left(\sum_{i=Al}^{Ni} y'_i \ln y'_i + \sum_{i=Ni}^{Va} y''_i \ln y''_i \right) \\ & + y'_{Al}y'_{Ni}L_{Al:Ni:*}^{AlNi} + y''_{Ni}y''_{Va}L_{*:Ni:Va}^{AlNi} \end{aligned} \quad (8)$$

Here, each of the G terms on the right, together with the two L terms, are temperature dependent coefficients, given by piecewise continuous expansions identical in form to that given in Equation (6), with each set of coefficients $a-h$ being obtained for SGTE. Although such expressions appear complex, particularly if more than one sublattice phase is present, as would be the case for growth of AlNi in an Al-rich liquid where the peritectic conversion to Al₃Ni₂ and subsequently Al₃Ni would need to be considered, the variational principles applied in phase-field simulation are well suited to the minimisation of such free energies.

Currently, we only apply the model to sublattice models in which the concentration c can be mapped uniquely onto a set of site occupancy fractions. Examples include AlNi (Al, Ni)(Ni, Va) and Al₃Ni₂ (Al)₃(Ni, Al)₂(Va, Ni) under the assumption that atoms always occupy their preferred lattice sites. Where this is not the case e.g. MgCu₂ (Mg, Cu)(Cu, Mg)₂, an additional closure condition would need to be included for the free energy minimisation.

2.2 Anti-Trapping Current for Arbitrary Thermodynamics

However, although minimisation of the complex free energies associated with sublattice phases is straightforward the solute trapping problems arising can be severe. For solidification of AlNi, with $c = 0.3$ (30% Ni) we measured the extent of solute trapping using the metric given in Equation (9):

$$\chi = 1 - \frac{\Delta c}{\Delta c_0} = 1 - \frac{|c_s^* - c_l^*|}{|c_s^E - c_l^E|} \quad (9)$$

For an undercooling of $\Delta T = 150$ K ($v = 0.001$ m s⁻¹) we found $\chi = 1.48\%$ at $\delta = 2d_0$ and $\chi = 1.74\%$ at $\delta = 4d_0$. Here d_0 is the chemical capillary length and is of the order of the interatomic spacing. At the high undercooling of 250 K ($v = 0.027$ m s⁻¹) the equivalent values were 2.01% and 2.45%. While such agreement may not seem amiss, the slope of the liquidus line for AlNi is 40 K/at%, wherein the tip undercooling is systematically in error by around 35-40% of the total undercooling due to solute trapping. This is despite the exceptionally low growth velocities in this system, both in the phase-field simulations and as measured experimentally [19].

To overcome the problems associated with such solute trapping we have proposed [20] a novel anti-trapping current based on an analytical model of a phase interface moving at fixed velocity \mathbf{u} , wherein the interface profile in a co-ordinate system co-moving with it will be:

$$\phi = \frac{1}{2} + \frac{1}{2} \tanh\left(\frac{2(\mathbf{x} - \mathbf{u}t) \cdot \hat{\mathbf{n}}}{\delta}\right) \quad (10)$$

where $\hat{\mathbf{n}}$ is the outward pointing normal to the interface. The corresponding steady-state solute field can be shown to be:

$$\dot{c} = -\nabla \cdot (D\nabla f_c + \mathbf{u}c) \quad (11)$$

Upon integration of Equation (11), and ignoring any fluxes that are tangential to the interface, we have:

$$0 = f_{cc} \nabla c \cdot \hat{\mathbf{n}} + f_{c\phi} \nabla \phi \cdot \hat{\mathbf{n}} + \frac{\mathbf{u} \cdot \hat{\mathbf{n}}}{D} (c - c_s^E) \quad (12)$$

where $f_{c\phi}$ is the mixed second derivative of f with respect to both c and ϕ . In order to ensure that c_l^* recovers c_l^E , i.e. to suppress solute trapping, we now rewrite Equation (12) introducing one additional degree of freedom, namely:

$$0 = (1 + \alpha) f_{c\phi} \nabla \phi \cdot \hat{\mathbf{n}} + \frac{\mathbf{u} \cdot \hat{\mathbf{n}}}{D} (c - c_s^e) \quad (13)$$

This is equivalent to postulating an anti-trapping current with the form:

$$\mathbf{j} = \alpha f_{c\phi} \nabla \phi \quad \text{with} \quad \alpha = -\frac{u(\Delta c_0)}{\left(D f_{c\phi} \nabla \phi \cdot \hat{\mathbf{n}}\right)_{x=x_{liq}}} + 1 \quad (14)$$

wherein, \mathbf{j} in Equation (14) can be evaluated for any free energy functional, subject only to it being differentiable with respect to c and ϕ .

In order to illustrate the efficacy of the anti-trapping current, Figure 1 shows the results for 3 simulations run at different interface width, each with and without the anti-trapping current. The simulation parameters are given in [20]. Figure 1a shows the evolution of the partition coefficient as a function of time from the start of the simulation, wherein it is apparent that

the application of the anti-trapping current renders the partitioning behaviour of the simulation independent of the interface width and ensures that the equilibrium partitioning behaviour (shown dotted) is recovered exactly. This is in distinct contrast to the simulations without the anti-trapping current, in which it is apparent that all interface widths significantly overestimate the partition coefficient, with the problem becoming progressively worse as the interface width increases. Figure 1 parts b & c show the corresponding growth velocity, V , and dendrite tip radius, ρ , as a function of simulation time. It is also apparent that with the anti-trapping current, all simulations are fully independent of the interface width, that is there is no interface width dependence in k_E , V , or ρ . Such interface width independence is not displayed by the simulations without anti-trapping, with the dendrite tip velocity systematically increasing with interface width. This is despite the fact that we use here an interface width much smaller than most phase field simulations reported in the literature ($d_0 = 1$ nm). We conclude that the inclusion of some form of anti-trapping current is essential to obtaining quantitative results in phase-field simulation and that the model presented here is the formulation appropriate to arbitrary CALPHAD thermodynamics without the use of interpolation polynomials.

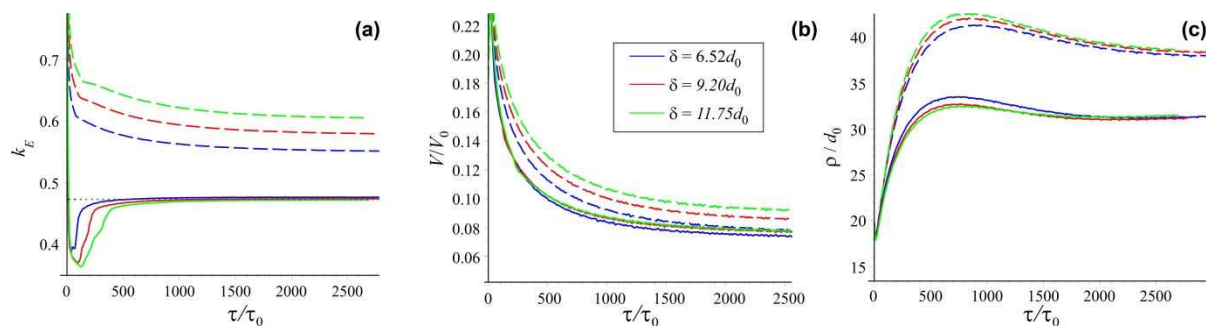


Figure 1. Comparison of (a) partition coefficient, (b) dendrite growth velocity and (c) dendrite tip radius as a function of time and interface width for phase-field simulations with (solid) and without (dashed) anti-trapping current.

2.3 Faceted Morphologies

The crystal morphology generated in the phase-field simulation is primarily determined by the growth anisotropy, which can be introduced via either the surface energy, γ , or the mobility M . The simplest, and most widely used, anisotropy in phase-field modelling is:

$$\gamma(\nabla\phi) = [1 + \varepsilon \cos 4\theta] \quad \text{with} \quad \hat{\mathbf{n}} \equiv \frac{\nabla\phi}{|\nabla\phi|} = \begin{bmatrix} \cos\theta \\ \sin\theta \end{bmatrix} \quad (15)$$

which results in (in 2-dimensions) four-fold symmetric dendritic growth. Here ε is a small parameter that controls the strength of the anisotropy. The equilibrium crystal morphology is given via the Wulff shape, $W(t) = [\gamma_x(t), \gamma_y(t)]$, where $[\phi_x = \cos(t), \phi_y = \sin(t)]$ and:

$$\gamma_x \equiv \frac{\partial \gamma}{\partial \phi_x}, \quad \gamma_y \equiv \frac{\partial \gamma}{\partial \phi_y} \quad (16)$$

It is well known that for four-fold growth the maximum value of ε that still permits all growth orientations is $\varepsilon < 1/15$. This corresponds to the interfacial stiffness, $\gamma_{\theta\theta} + \gamma$, being strictly > 0 . For $\varepsilon > 1/15$ some growth orientations become disallowed, wherein the Wulff shape develops cusps, as shown in Figure 2. It is often assumed that this will give faceted growth, but in fact this is not the case and as can be seen from Figure 2 the equilibrium morphology will actually have pointed corners (resulting from the disallowed growth directions) but curved sides.

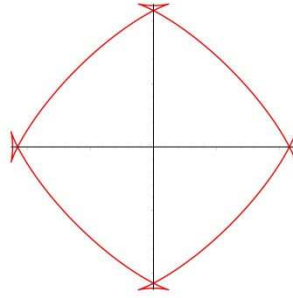


Figure 2. Wulff shape for a four-fold anisotropy with $\varepsilon > 1/15$. Cusp indicate disallowed growth directions in the resulting crystal morphology.

In fact, the appropriate form of the anisotropy functional to obtain straight sides (i.e. facets) can be found from $W(t)$ to be of the form $(1 + |\varepsilon \cos(n\theta)|)$, where n is an integer that will give a crystal with $2n$ -fold symmetry, i.e. $(1 + |\varepsilon \cos(3\theta)|)$ would give a hexagonal crystal. The resulting crystal morphology would however still have sharp corners: this is not conducive to computation via phase-field. To ‘regularise’ the shape we approximate $|\cos(3\theta)|$ by $\sqrt{(\cos 3\theta)^2 + q}$, where q is a small parameter, **which in the simulations presented below is taken as 0.2. The effect of the value of q on the interface stiffness is discussed in [21].**

Noting that $\cos 3\theta = \cos^3 \theta - 3\cos \theta \sin^2 \theta$, the form of the anisotropy functional used in the model becomes:

$$\gamma = \left\{ 1 + \varepsilon \sqrt{\frac{(\phi_x^3 - 3\phi_x \phi_y^2)^2 + q^6}{(\phi_y^2 + \phi_y^2 + q^2)^3}} \right\} \quad (17)$$

By introducing the faceting behaviour into the surface energy we are able to show that the model has the following interesting property: close to equilibrium the fully faceted morphology is produced (i.e. that, as expected, the Wulff shape is recovered) but that with larger departures from equilibrium a more continuous, dendritic morphology is obtained. This is illustrated in Figure 3. Figure 3a shows the crystal morphology at low undercooling,

wherein the faceted hexagonal morphology of the Wulff shape is exactly recovered. At intermediate undercooling (Figure 3b) a transitional morphology, that of a faceted dendrite, is obtained while at high undercooling (Figure 3c) a continuous six-fold symmetric dendrite is obtained. Also shown in Figure 3c are contours from throughout the growth so that the evolution of the shape, from initial hexagonal seed to fully continuous dendrite may be observed. The transition of the growth morphology from faceted to continuous with increasing departure from equilibrium is considered a desirable property of the model that closely mimics just such a transition observed in rapid solidification experiments [22, 23, 24].

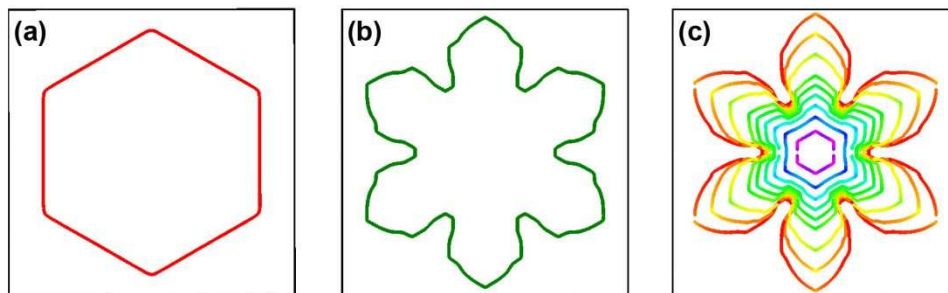


Figure 3. Growth morphologies produced by the anisotropy functional given by Equation (17). (a) at low undercooling, wherein the faceted hexagonal morphology of the Wulff shape is recovered, (b) faceted dendrite at intermediate undercooling and (c) fully continuous dendrite at large undercooling.

3.0 Discussion and Summary

We present what essentially is the toolbox for the simulation of intermetallic compounds during alloy solidification. Moreover, all of the proposed modifications can be implemented so as to run alongside a standard phase-field model for solution phases with a continuous interface. As such, the simulation of faceted intermetallic phases growing contemporaneously with a continuous solution phase becomes feasible.

4.0 Acknowledgements

This research was funded by EPSRC Innovative Manufacturing Research Hub in Liquid Metal Engineering (LiME), Grant No. EP/N007638/1.

5.0 References

1. SGTE - Scientific Group Thermodata Europe, see www.sgte.net/en/about-sgte.
2. Choudhury A, Kellner M, Nestler B, *Curr. Opin. Solid State Mater. Sci.* **19** (2015) 287.
3. Ohno M, Takaki T, Shibuta Y, *Phys. Rev. E* **96** (2017) 33311.

4. Taylor J E, Cahn J W, *Physica D* **112** (1998) 381.
5. Eggleston J J, McFadden G B, Voorhees P W, *Physica D* **150** (2001) 91.
6. Debierre J-M, Karma A, Celestini F, Guerin R, *Phys. Rev. E* **68** (2003) 041604.
7. Choi J, Park S-K, Hwang H-Y, Huh J-Y, *Acta Mater.* **84** (2015) 55.
8. Abinandanan T A, Haider F, *Phil. Mag. A* **81** (2001) 2457.
9. Nani E S, Gururajan M P, *Phil. Mag.* **94** (2014) 3331.
10. Karma A, *Phys. Rev. Lett.* **87** (2001) 115701.
11. Galenko P K, Abramova E V, Jou D, Danilov D A, Lebedev V G, Herlack D M, *Phys. Rev. E* **84** (2011) 041143.
12. Mullis A M, *Int. J. Heat Mass Transfer* **40** (1997) 4085.
13. Zhang L, Danilova E V, Steinbach I, Medvedev D, Galenko, P K, *Acta Mater.* **61** (2013) 4155.
14. Bollada P C, Jimack P K, Mullis A M, *Comp. Mater. Sci.* **126** (2016) 426.
15. Bollada P C, Goodyer C E, Jimack P K, Mullis A M, Yang F W, *J. Comp. Phys.* **287** (2015) 130.
16. Brandt A, *Math. Comput.* **31** (1977) 333.
17. MacNeice P, Olson K M, Mobarry C, de Fainchtein R, Packer C, *Comput. Phys. Commun.* **126** (2000) 330.
18. Redlich O, Kister A, *Indust. Eng. Chem.* **40** (1948) 345.
19. Lengsdorf R, Holland-Moritz D, Herlach D M, *Acta Mater.* **62** (2009) 365.
20. Bollada P C, Jimack P K, Mullis A M, *Comp. Mater. Sci.* **151** (2018) 338.
21. Bollada P C, Jimack P K, Mullis A M, *Comp. Mater. Sci.* **144** (2018) 76.
22. Liu R B, Herlach D M, Vandyousse M, Greer A L, *Metal. Mat. Trans A* **35** (2003) 1067.
23. Battersby S E, Cochrane R F, Mullis A M, *Mater. Sci. Eng., A* **226** (1997) 443.
24. Battersby S E, Cochrane R F, Mullis A M, *J. Mater. Sci.* **34** (1999) 2049.